Korean J. Chem. Eng., 37(8), 1427-1435 (2020)
DOI: 10.1007/s11814-020-0577-3

pISSN: 0256-1115
eISSN: 1975-7220

Hydrogen storage into monobenzyltoluene over Ru catalyst supported on SiO_2-ZrO_2 mixed oxides with different Si/Zr ratios

Tae Wan Kim*, Chansong Kim, Hwiram Jeong*, Chae-Ho Shin**, and Young-Woong Suh*,***,†**

*Department of Chemical Engineering, Hanyang University, Seoul 04763, Korea
**Department of Chemical Engineering, Chungbuk National University, Chungbuk 28644, Korea
***Research Institute of Industrial Science, Hanyang University, Seoul 04763, Korea

(*Received 1 April 2020 • Revised 29 April 2020 • Accepted 11 May 2020*)

Abstract−Supported Ru catalysts have been often employed for hydrogen charge into liquid organic hydrogen carrier molecules (monobenzyltoluene in this work), and their catalytic performance largely depends upon physicochemical properties of the support materials. We prepared supported Ru catalysts on SiO_2-ZrO_2 with different Si/(Si+Zr) ratios ranging from 0 to 30 mol% by loading $Ru_3(CO)_{12}$ onto Si,Zr-mixed metal hydroxide and subsequent thermolysis. The textural properties, Ru particle size, and hydrogenation activity of Ru/SiO_2-ZrO_2 catalysts show a volcano-shaped dependence on the content of Si added, where the maximum is achieved at the Si/(Si+Zr) ratio of 5 mol%. Up to this Si content the incorporation of Si into ZrO_2 improves thermal stability and decreases the particle size of tetragonal ZrO_2, resulting in a positive contribution to hydrogen storage efficiency. However, the further addition of Si increases surface heterogeneity and charge imbalance, and hence induces a decrease in the density of surface OH group reacting with $Ru_3(CO)_{12}$, which explains the lowered activity. Therefore, the addition of up to 5 mol% Si into ZrO_2 is effective in enhancing the hydrogenation performance of Ru/ZrO_2 owing to the improved textural properties and smaller Ru particles.

Keywords: Liquid Organic Hydrogen Carrier, Hydrogen Storage, Supported Ru Catalysts, Silica-zirconia Mixed Oxide

INTRODUCTION

Liquid organic hydrogen carrier (LOHC) systems have attracted tremendous attention for hydrogen storage and transport in recent years. The benefits of LOHC systems include fair compatibility with the existing crude oil infrastructure, long-term hydrogen storage without any loss, high-purity hydrogen release, and integration with fuel-cell systems [1-5]. LOHC systems are based on a pair of hydrogen-lean organic compounds and the corresponding hydrogenation products; e.g., a pair of aromatic and alicylcic molecules, and a pair of heteroaromatic and heterocyclic ones. Hydrogen is stored by the hydrogenation of H_2-lean compounds and reversibly released by the dehydrogenation of H_2-rich compounds [6-8]. For suitable LOHC compounds, the following properties are required: low melting point (<−30 °C), high boiling point (>270 °C), high H_2 storage capacity (>6 wt%), sufficeint volumetric energy density (>1.7 kWh/L), non-toxicity, low product price, and high stability in the reversible hydrogenation and dehydrogenation reactions [6,9,10].

In this respect, monobenzyltoluene (H_0-MBT) and dibenzyltoluene (H_0-DBT), which are well-known heat-transfer fluids (e.g., Marlotherm® LH and SH as Sasol's trade name, respectively), are very promising LOHC compounds with the following properties: H_2 storage capacity of 6.2 wt%, energy density of 1.9 kWh/L, availability at a relatively low price (US $4 per kg H_0-DBT), excellent thermal stability and reversibility, and favorable thermophysical properties for safe handling (boiling point: H_0-DBT 390 °C, H_0-MBT 280 °C and melting point: H_0-DBT −48 °C, H_0-MBT −30 °C) [3,9-11]. Although H_0-DBT exhibits superior thermophysical characters, H_0-MBT with three stereoisomers of *ortho*-, *meta*-, and *para*-form has been often used for precise evaluation of LOHC performance [12,13]. While the dehydrogenation reaction requires a number of elegant catalyst works due to its endothermic nature [14-17], a study to find an active hydrogenation catalyst has been rarely conducted despite some recent reports on the effects of the impurities in hydrogen (e.g., CO, CO_2, CH_4, and H_2O) on the catalytic hydrogenation performance [18-21].

Supported Ru catalysts have been frequently employed in the hydrogenation of diverse LOHC compounds owing to excellent hydrogenation performance and lower price of Ru compared to Pt, Pd, and Rh [11,22-24]. Among several Ru precursors, $Ru_3(CO)_{12}$ was evaluated to be the best in terms of the Ru dispersion and hydrogenation performance [13,25,26]. The quality of final Ru catalysts synthesized from $Ru_3(CO)_{12}$ is strongly influenced by the nature and properties of metal oxide supports in the impregnation and thermolysis processes [27-31]. We also confirmed that the hydrogenation activity, Ru particle size, and quantity of surface Ru were determined by the textural and surface properties of the support interacting with $Ru_3(CO)_{12}$ [13,26,32]. In particular, when $Ru_3(CO)_{12}$ was loaded onto zirconium hydroxide, the medium density of surface OH group was found to be adequate for the smallest Ru particle and highest hydrogenation activity [26].

ZrO_2 is an attractive support with strong-metal support interaction, high thermal stability, and acid-base properties [33]. Therefore, ZrO_2-supported Ru catalysts were applied for partial hydrogenation

---

[†] To whom correspondence should be addressed.
E-mail: ywsuh@hanyang.ac.kr

of benzene [34,35]. Meanwhile, since tetragonal ZrO_2 generally exhibits a higher BET surface area, more acidity, and smaller particle size than monoclinic ZrO_2, metal catalysts supported on the former phase were examined to display higher activity than that supported on the latter phase [36,37]. Interestingly, the incorporation of Si into ZrO_2 was reported to enhance thermal stability of tetragonal ZrO_2 and suppress the nucleation and growh of ZrO_2 [38-41]. Based on these features, SiO_2-ZrO_2 mixed oxides have been employed as a support in numerous chemical reactions, such as CO hydrogenation [42], CO methanation [43], CH_4 reforming [44,45], hydrodeoxygenation [46,47]. This motivated us to develop a more active SiO_2-ZrO_2-supported Ru catalyst than ZrO_2-supported one that was previously studed in the hydrogenation of H_0-MBT [26]. The textural and surface properties modified by the incorporation of Si into ZrO_2 may affect the interaction of SiO_2-ZrO_2 with $Ru_3(CO)_{12}$. Hence, the properties and hydrogenation activity of Ru/SiO_2-ZrO_2 catalysts would vary depending on the molar ratio of Si/(Si+Zr).

In this work, we prepared Si,Zr-mixed metal hydroxide samples with different Si/(Si+Zr) ratios by hydrothermal synthesis using a Teflon-lined stainless steel autoclave. Note that the applied preparation method can help in achieving an accurate Si content, since SiO_2 is slowly dissolved from the Pyrex or quartz glass vessel while the precipitation of metal hydroxide(s) proceeds under high pH using alkaline solution [48,49]. The dried mixed metal hydroxide samples then reacted with $Ru_3(CO)_{12}$ followed by thermolysis at 700 °C, yielding the final SiO_2-ZrO_2-supported Ru catalysts. These catalysts were tested in the hydrogenation of H_0-MBT under different reaction conditions to estimate H_2 storage efficiency and kinetic parameters. The activity results were discussed from various characteristics of Ru/SiO_2-ZrO_2 catalysts and also from the properties of the prepared support materials, which reveals the optimal Si/(Si+Zr) ratio for superior hydrogenation performance of Ru/SiO_2-ZrO_2 catalyst. Consequently, we could address the effects of Si incorporation into ZrO_2 on crucial characteristics of Ru catalyst supported on SiO_2-ZrO_2 in the hydrogenation of LOHC compounds.

EXPERIMENTAL

1. Synthesis of Si,Zr-containing Samples

Hydrothermal syntheis was used for the preparation of Si,Zr-containing samples with the different Si/(Si+Zr) ratio ranging from 0 to 30 mol%. Typically, an aqueous ammonia solution of 2 M (Samchun Chemicals, 28 wt% NH_4OH) was added dropwise into an aqueous $ZrO(NO_3)_2 \cdot 2H_2O$ solution of 0.5 M (KANTO Chemicals, 99%) with the desired amount of 10 vol% tetraethyl orthosilicate solution (Acros Organics, 98%) in ethanol until a pH value finally approached 10. Then, a portion of the suspension (280 ml) was loaded into a Teflon-lined stainless steel autoclave and aged at 100 °C for 24 h with stirring of 60 rpm. After cooling to room temperature, the resulting product was centrifuged at 3,000 rpm for 30 min and dried at 60 °C for 24 h followed by additional drying at 105 °C overnight. The dried samples are labelled herein as SZ-*x*-d, where *x* indicates the molar percentage of Si/(Si+Zr). Additionally, a portion of SZ-*x*-d sample was thermally treated at 700 °C for 3 h in a H_2 flow (100 cm^3 min^{-1}), which is named SZ-*x*-H_2-700.

2. Preparation of Ru/SiO_2-ZrO_2 Catalysts

To prepare supported Ru catalysts, the aforementioned SZ-*x*-d samples were in contact with a solution of $Ru_3(CO)_{12}$ (Sigma-Aldrich Chemical Co., 99%) in tetrahydrofuran (Daejung Chemicals, 99.5%) to achieve the nominal Ru loading of 3.8 wt%. After stirring at room temperature, the solvent was removed at 45 °C at a reduced pressure. The resulting samples were dried at 105 °C for 8 h, which is labelled as $Ru_3(CO)_{12}$/SZ-*x*-d. Ru/SiO_2-ZrO_2 catalysts (denoted as Ru/SZ-*x*) were finally obtained by thermolysis of $Ru_3(CO)_{12}$/SZ-*x*-d samples under the same conditions as for SZ-*x*-H_2-700 samples.

3. Sample Characterization

Powder X-ray diffraction (XRD) analysis involved using a Rigaku MiniFlex600 diffractometer with a Cu Kα radiation source operated at 40 kV and 15 mA. All diffraction patterns were recorded in the 2θ range of 10 to 90° at a scan rate of 10° min^{-1} with a step of 0.02°. N_2 physisorption was performed at 77 K using a Micromeritics ASAP 2020 instrument after the pretreatment of a sample (100 mg) at 105 °C for 1 h under vacuum. The actual Ru loading was measured with an inductively coupled plasma optical emission spectrometer (ICP-OES) using a Thermo Scientific iCAP 7000 series, where a sample was dissolved in a mixture of nitric acid and hydrochloric acid (1 : 6, v/v) followed by the pretreatment in a Milestone Ethos Easy Microwave digestion system. X-ray photoelectron spectroscopy (XPS) spectra were collected using a Thermo Scientific K-alpha plus spectrometer with a monochromatic Al Kα X-ray source of 1,486.6 eV, where all spectra were obtained with a pass energy of 50 eV and an energy step size of 0.1 eV and then calibrated by a standard C 1s binding energy of 284.6 eV. High resolution transmission electron microscopy (HR-TEM) and transmission electron microscope equipped with an energy-dispersive X-ray spectrometer (TEM-EDS) images were taken in a JEOL JEM-2100F microscope operated at an acceleration voltage of 200 kV, where the specimen was prepared by dropping a sample in methanol onto a 300-mesh copper grid and then drying at 60 °C under vacuum overnight.

Fourier-transform infrared (FT-IR) spectra were collected using a Thermo Scientific Nicolet 6700 spectrometer equipped with a MCT-A detector, where a sample (100 mg) mixed with as-prepared sample and KBr (1 : 10, w/w) was pelletized into a circular flat disk of 0.65 cm radius and pretreated at 105 °C for 1 h under vacuum in a quartz IR cell. Then, the spectrum was recorded in the wavenumber range of 1,200 to 700 cm^{-1} with a scan number of 64 and a resolution of 4 cm^{-1}. Differential scanning calorimetry (DSC) measurement was conducted using a TA Instrument SDT Q600 thermal analyzer, where a sample (5 mg) was loaded onto alumina pan and heated to 1,000 °C (ramping rate: 10 °C min^{-1}) under an air flow (100 cm^3 min^{-1}). Temperature-programmed reduction coupled with mass spectroscopy (TPR-MS) experiments was carried out using a BELCAT-B instrument coupled with a quadrupole mass spectrometer (BEL-MASS) operated at a voltage of 1,200 V, where a sample (50 mg) was heated to 550 °C (ramping rate: 5 °C min^{-1}) in a 10% H_2/Ar flow (30 cm^3 min^{-1}), while the mass signal of m/z= 2 for the evolution of H_2 was detected. CO chemisorption was performed using a BELCAT-B instrument, where a sample (50 mg) was pretreated at 250 °C (ramping rate: 5 °C min^{-1}) for 1 h in a 10% H_2/Ar flow (30 cm^3 min^{-1}) followed by cooling to 30 °C in a

He flow (30 cm^3 min^{-1}). Then, a pulse of 5% CO/He gas was repeatedly injected until the peak area was saturated, while the applied assumptions were a spherical particle geometry and a stoichiometry of CO/Ru=1 : 1.

4. Catalytic Activity Test in the Hydrogenation of H_0-MBT

The reactant H_0-MBT consisting of diphenylmethane impurity (H_0-DPM), *meta* H_0-MBT, *ortho* H_0-MBT, and *para* H_0-MBT with the molar percentages of 0.9 : 5.0 : 45.6 : 48.5 was supplied by Samyang Oil Company in South Korea (Sasol Marlotherm® LH Charge-No. 1717), as described in our previous report [13]. The hydrogenation of H_0-MBT was conducted in a Parr reactor with a glass liner (volume 100 cm^3) using two different approaches, schematically depicted in Fig. S1, to evaluate the performance of Ru/SZ-*x* catalysts in terms of the hydrogenation products and consumed H_2.

In the first way (reaction system A), H_0-MBT (15 g) and Ru/SZ-*x* catalyst (120 or 200 mg) were loaded into the reactor. The reactor was purged with 99.99% H_2 for 5 min and pressurized to 50 bar, which was maintained for the entire reaction course using a back pressure regulator, followed by heating to the desired temperature (150 or 170 °C). After the reaction for 2 h with the stirring rate of 1,200 rpm, the reactor was cooled to ambient temperature without stirring. The obtained product (1 g) was filtered with a syringe filter (0.1 μm) and mixed with a solvent (10 mL acetone) and an internal standard (100 μL nonane). An aliquot of this mixture was analyzed using a gas chromatograph (GC; Agilent Technologies 7890A) equipped with an auto-sampler, a flame ionization detector, and a Restek Rxi®-17Sil MS column (30 m×0.25 mm×0.25 μm). The condition for GC analysis was as follows: injector temperature=300 °C, detector temperature=300 °C, flow rate=0.2 cm^3 min^{-1}, split ratio=1 : 300, and oven program: 50 °C→ramping with 50 °C min^{-1}→140 °C for 80 min→ramping with 50 °C min^{-1} →250 °C for 5 min. The moles of H_0-MBT and H_{12}-MBT were calculated based on their measured calibration factor (CF) values, whereas the moles of H_4-MBT and H_6-MBT were calculated from the CF value of H_0-MBT and that of H_{10}-MBT was quantified from that of H_{12}-MBT since the pure reaction intermediates (H_4-MBT, H_6-MBT, and H_{10}-MBT) were not available [13]. The conversion of H_0-MBT, product selectivities, and H_2 storage efficiency were calculated using the following equations:

Conversion of H_0-MBT (mol%)
=(initial H_0-MBT [mol]−final H_0-MBT [mol])/
(initial H_0-MBT [mol])×100%
Selectivity to H_x-MBT (mol%)
=(final H_x-MBT [mol])/(final H_{12}-MBT [mol]
+final H_{10}-MBT [mol]+final H_6-MBT [mol]
+final H_4-MBT [mol])×100%
H_2 storage efficiency (%)
={(final H_{12}-MBT [mol]×6H_2)+(final H_{10}-MBT [mol]×5H_2)
+(final H_6-MBT [mol]×3H_2)+(final H_4-MBT [mol]×2H_2)}
/(initial H_0-MBT [mol]×6H_2)×100%

To measure H_2 consumption in gas phase, the reactor was connected to a Parr high-pressure gas burette filled with 99.99% H_2. This reaction system B can be operated at constant pressure in the entire reaction course by continuously feeding H_2 from the gas burette as much as the consumed H_2. The reactor with H_0-MBT (10 g) and Ru/SZ-*x* catalyst (200 mg) was purged with H_2 three times and pressurized to 5 bar. After the reaction mixture approached a desired temperature (170, 190, or 210 °C) and H_2 was then fed to 50 bar, the reaction was conducted until no pressure change in the gas burette was observed, while the pressure of H_2 in the gas burette was recorded in real time. Since the hydrogenation of H_0-MBT to H_{12}-MBT is a consecutive reaction via the above-mentioned reaction intermediates [12], the consumption of H_2, equivalent to H_2 conversion (X_{H_2}), was calculated as follows:

H_2 consumption (%)=(mole of H_2 consumed in the burette)/
[(initial mole of H_2 in the burette)−
(final mole of H_2 when no pressure change is observed in the burette)]
×100%

RESULTS AND DISCUSSION

1. Formation of Zr-O-Si Bond in the Si,Zr-containing Samples

The XPS Zr 3d and Si 2p spectra of SZ-*x*-d samples show the formation of more Zr-O-Si bonds with increasing the Si content. The binding energy of Zr $3d_{5/2}$ increases from 182.1 eV for SZ-0.0-d to 182.3 eV for SZ-30.0-d, while that of Si 2p is shifted towards higher values (cf. 103.2 eV for pure SiO_2), due to higher electronegativity of Si (1.90) than Zr (1.33) (Fig. S2(a), (b)) [50,51]. The FT-IR spectra of SZ-*x*-d samples also represent the formation of Zr-O-Si bonds by the broad band around 1,000 cm^{-1} with the incorporation of Si into ZrO_2. This band is gradually shifted to higher wavenumers as the Si content is increased (Fig. S2(c)), indicating the increased formation of Zr-O-Si and Si-O-Si bonds (cf. 1,100 cm^{-1} for pure SiO_2) [52-54].

Moreover, Ru/SZ-*x* catalysts display the same trends as SZ-*x*-d samples in the XPS Zr 3d and Si 2p spectra, meaning that Zr-O-Si bonds are more formed as the Si content increases. Especially, the peak shift observed in Ru/SZ-*x* catalysts is more noticeable than that in SZ-*x*-d samples (Fig. S3).

Additionally, the elemental composition of SZ-*x*-H_2-700 samples was determined by ICP-OES, TEM-EDS, and XPS analysis (Table 1). The bulk molar percentage of Si/(Si+Zr) appears to be very close to the nominal value in all the samples. However, the XPS results reveal that the element Si is enriched at the external surface, due to slower condensation of Si moiety than Zr one in the synthesis [38,41]. Similar results are found in the elemental compositions of Ru/SZ-*x* catalysts.

2. Hydrogenation Activities of Ru/SiO_2-ZrO_2 Catalysts

The prepared Ru/SZ-*x* catalysts with the same actual Ru loading (Table 1) were tested in the hydrogenation of H_0-MBT at 50 bar H_2 for 2 h in the reaction system A. When the catalyst amount of 200 mg and temperature of 170 °C were employed for the reaction, the H_2 storage efficiency, calculated from the liquid products after the reaction, showed a volcano-shaped dependence on the Si content at the maximum of 97.2% with Ru/SZ-5.0 (Fig. 1). This tendency was similar when the catalyst amount decreased to 120 mg and even when the temperature decreased to 150 °C, although the activity difference was smaller. In more detail, both the conversion of H_0-MBT and selectivity to H_{12}-MBT follow the same trend as the H_2 storage efficiency, as summarized in Table S1.

Table 1. Elemental compositions of SZ-*x*-H_2-700 samples and Ru/SZ-*x* catalysts

Sample	Ru [wt%][a]	Si/(Si+Zr) [mol%][b]	Si/(Si+Zr) [at%][c]	Si/(Si+Zr) [at%][d]	O/(Si+Zr) [at%][e]
SZ-0.0-H_2-700		0.0	0.0	0.0	2.5
SZ-1.25-H_2-700		1.0	0.7	5.2	2.5
SZ-2.5-H_2-700		2.2	2.0	8.3	2.5
SZ-5.0-H_2-700		4.8	4.8	11.1	2.5
SZ-10.0-H_2-700		9.0	9.5	17.1	2.4
SZ-30.0-H_2-700		28.0	29.6	38.3	2.4
Ru/SZ-0.0	3.8	0.0	0.0	0.0	2.7
Ru/SZ-1.25	3.8	1.0	0.8	6.4	2.7
Ru/SZ-2.5	3.8	2.1	2.4	8.5	2.7
Ru/SZ-5.0	3.8	4.5	4.6	14.7	2.7
Ru/SZ-10.0	3.8	8.3	8.6	23.5	2.7
Ru/SZ-30.0	3.8	27.9	28.4	39.1	2.7

[a] Actual Ru loading measured by ICP-OES analysis.
[b] Ratio of Si to (Si+Zr) measured by ICP-OES analysis.
[c] Ratio of Si to (Si+Zr) determined by the TEM-EDS.
[d] Ratio of Si to (Si+Zr) calculated from the XPS results.
[e] Ratio of O to (Si+Zr) calculated from the XPS results.

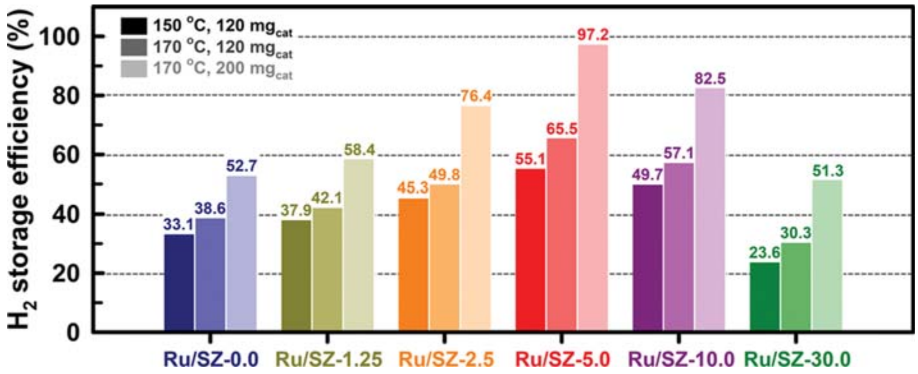

Fig. 1. H_2 storage efficiency of Ru/SZ-*x* catalysts using the reaction system A. Reaction conditions: 15 g H_0-MBT, 50 bar H_2, 1,200 rpm, and 2 h.

H_2 consumption in the hydrogenation of H_0-MBT was measured using the reaction system B that was operated at 50 bar H_2 and 200 mg catalyst. From the H_2 consumption curves in Fig. S4, the measured time to fully charge H_2 into H_0-MBT at all the tested temperatures (170, 190, and 210 °C) exhibits an inverse volcano-shaped dependence on the Si content at the minimum with Ru/SZ-5.0 (Fig. 2(a)). This suggests that the fastest H_2 charge is possible with Ru/SZ-5.0. Furthermore, the first-order rate constant (k) was calculated from the plot of $\ln(1-X_{H_2})$ against the reaction time when the conversion of H_2 (X_{H_2}) was below 30% (Fig. S5). The value of k shows a volcano-shaped dependence on the Si content (Fig. 2(b)), as observed in H_2 storage efficiency. We also calculated the activation energy (E_a) from the Arrhenius plot using the k values obtained at three different temperatures. As a result, the value of E_a follows a similar trend as shown in Fig. 2(a). Therefore, the activity results determined from the two reaction systems indicate that the increase in the Si content up to 5 mol% (i.e., SZ-5.0) has a positive effect on the hydrogenation performance of Ru/SZ-*x* catalyst, but further addition of Si does not make a good contribution to the catalytic activity.

3. Characteristics of Ru/SiO_2-ZrO_2 Catalysts

Table 2 lists various physicochemical properties of Ru/SZ-*x* catalysts to support the obtained hydrogenation activity results. The Ru particle size determined from the TEM images (Fig. 3) increases in the following order: Ru/SZ-5.0 (1.40 nm)<Ru/SZ-10.0 (1.57 nm)<Ru/SZ-2.5 (1.63 nm)≈Ru/SZ-30.0 (1.65 nm)<Ru/SZ-1.25 (1.81 nm)<Ru/SZ-0.0 (2.16 nm). When the experiment of CO chemisorption was conducted to access the volume of CO adsorbed onto Ru particles, a similar trend was also noticed in this order: Ru/SZ-5.0 (0.32 cm^3 g^{-1})>Ru/SZ-10.0 (0.24 cm^3 g^{-1})>Ru/SZ-2.5 (0.19 cm^3 g^{-1})>Ru/SZ-30.0 (0.13 cm^3 g^{-1})>Ru/SZ-1.25 (0.08 cm^3 g^{-1})>Ru/SZ-0.0 (0.03 cm^3 g^{-1}). These results are in good agreement with the hydrogenation activity, except Ru/SZ-30.0 showing the lowest hydrogenation activity among the tested Ru/SZ-*x* catalysts. This is due to rod-like ZrO_2 structure formed on the catalyst surface, which is seen from the inset in the HR-TEM image of Ru/SZ-30.0. TEM-EDS mapping images also identify the absence of Ru in the rod-like ZrO_2 (Fig. S6). Since this rod-like ZrO_2 is not observed in the

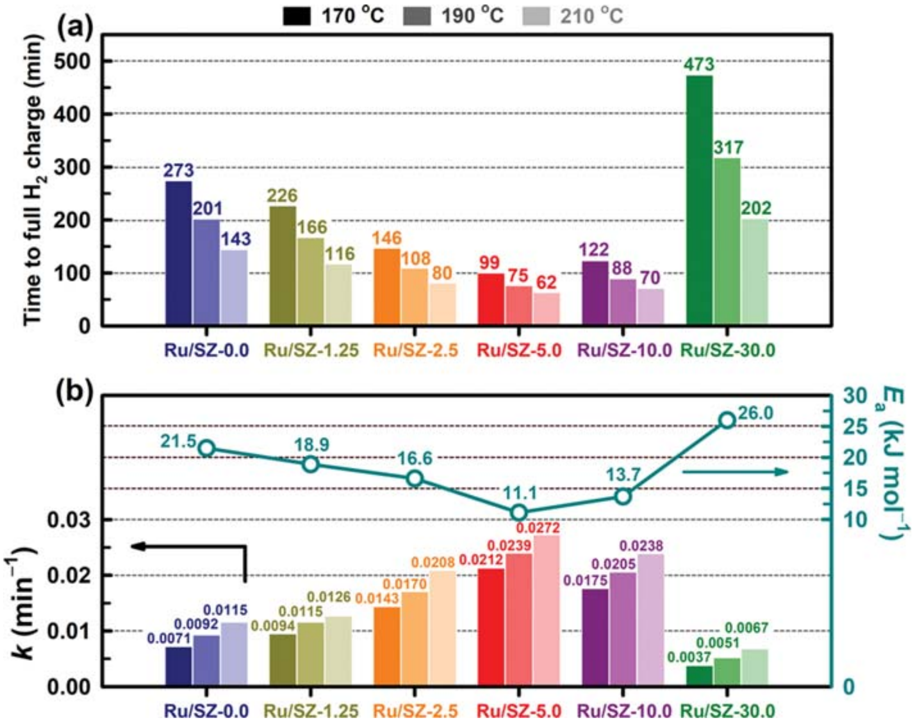

Fig. 2. Hydrogenation performance of Ru/SZ-*x* catalysts using the reaction system B: (a) Time to full H_2 charge into H_0-MBT and (b) calculated kinetic parameters, *k* and E_a. Reaction conditions: 10 g H_0-MBT, 200 mg_{cat}, 50 bar H_2, and 1,200 rpm.

Table 2. Physicochemical properties of Ru/SZ-*x* catalysts

Sample	S_{BET}^{a} [m^2 g^{-1}]	V_p^{a} [cm^3 g^{-1}]	d_p^{a} [nm]	$D_{m\text{-}ZrO_2}^{b}$ [nm]	$D_{t\text{-}ZrO_2}^{b}$ [nm]	n_{CO}^{c} [cm^3 g^{-1}]	D_{Ru}^{d} [nm]	Ru/(Si+Zr)^{e} [at%]
Ru/SZ-0.0	4	0.016	17.3	25.9	23.4	0.03	2.16±0.72	8.05
Ru/SZ-1.25	9	0.033	15.0	21.9	20.7	0.08	1.81±0.49	6.39
Ru/SZ-2.5	15	0.049	12.5	-	19.1	0.19	1.63±0.47	5.72
Ru/SZ-5.0	33	0.077	9.2	-	17.4	0.32	1.40±0.36	5.00
Ru/SZ-10.0	23	0.056	8.5	-	16.9	0.24	1.57±0.53	4.79
Ru/SZ-30.0	21	0.034	6.6	-	13.7	0.13	1.65±0.37	4.48

[a] BET surface area (S_{BET}), pore volume (V_p), and pore diameter (d_p) measured by N_2 physisorption at 77 K.
[b] Particle size of monoclinic ZrO_2 ($D_{m\text{-}ZrO_2}$) and tetragonal ZrO_2 ($D_{t\text{-}ZrO_2}$) calculated by the Scherrer's equation.
[c] CO adsorption volume measured by CO chemisorption (CO : Ru=1/1).
[d] Ru particle size determined by statistical analysis of about 100 particles from TEM images.
[e] Surface atomic ratio of Ru to (Si+Zr) calculated from the XPS results.

TEM image of SZ-30.0-H_2-700 (Fig. S7), it can be suggested that strong interaction between Ru and SiO_2 pushes the ZrO_2 domain to the external surface, followed by aggolmeration of ZrO_2 into a rod-like structure.

It is found from the XRD patterns of Ru/SZ-*x* catalysts that the phase of ZrO_2 varies with increasing the Si content, while Ru-related diffraction peaks are not detected due to fine Ru nanoparticles (Fig. 4). Ru/SZ-0.0 and Ru/SZ-1.25 appear as monoclinic zirconia phase (*m*-ZrO_2) together with tetragonal phase (*t*-ZrO_2), whereas only *t*-ZrO_2 is noticed from Ru/SZ-2.5 to Ru/SZ-30.0. Also, the particle size of *t*-ZrO_2 steadily decreases from 23.4 nm (Ru/SZ-0.0) to 13.7 nm (Ru/SZ-30.0). This is due to the formation of Zr-O-Si bonds by the incorporation of Si into ZrO_2, leading to enhanced stability of *t*-ZrO_2 [39,55-57]. For confirmation, the temperature of the glow exotherm was identified by DSC measurement for SZ-*x*-d samples (Fig. S8). The crystallization temperature is shifted to higher temperature in the following order: 436 °C (SZ-0.0-d)< 459 °C (SZ-1.25-d)<482 °C (SZ-2.5-d)<534 °C (SZ-5.0-d)<615 °C (SZ-10.0-d)<824 °C (SZ-30.0-d). Therefore, the thermal stability of SZ-*x*-d samples is improved by the increase in the Si content.

Textural properties such as BET surface area and pore volume were investigated for Ru/SZ-*x* catalysts. With increasing the Si content, the BET surface area increased from 4 m^2 g^{-1} (Ru/SZ-0.0) to 33 m^2 g^{-1} (Ru/SZ-5.0), and then decreased to 21 m^2 g^{-1} (Ru/SZ-30.0). The same trend is observed in the pore volume. Meanwhile, hysteresis progressively shifted toward lower relative pressure and the pore diameter continuously decreased from 17.3 to 6.6 nm with increasing the Si content (Fig. S9), due to the microporous character of

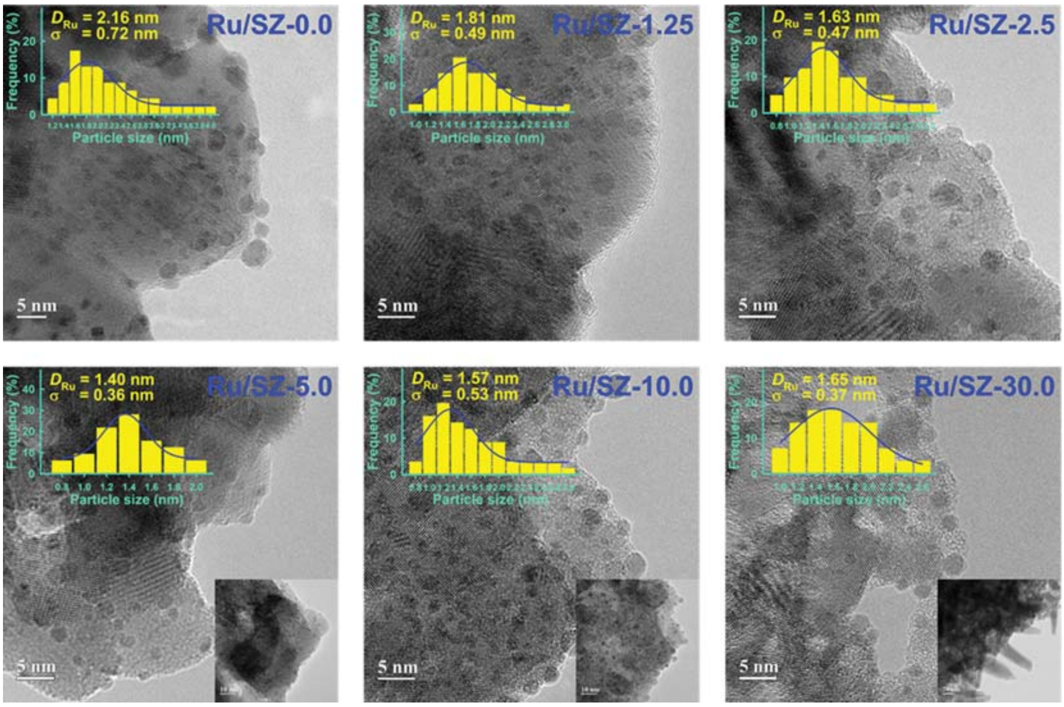

Fig. 3. HR-TEM images and Ru particle size distributions of Ru/SZ-*x* catalysts. The average particle size and standard deviation are noted in each micrograph.

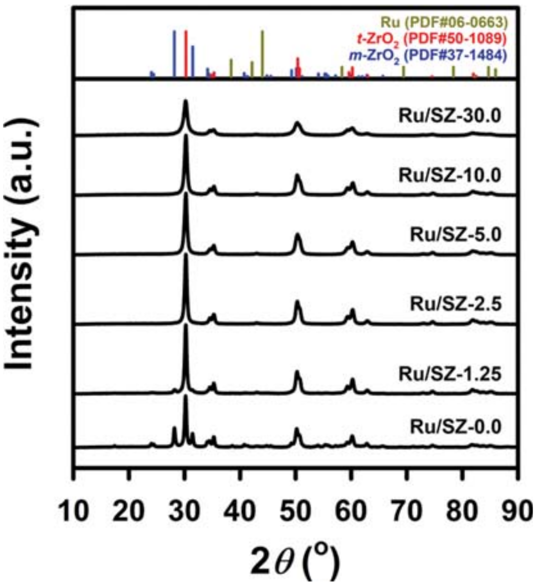

Fig. 4. XRD patterns of Ru/SZ-*x* catalysts. The standard reflections of *m*-ZrO_2 (PDF #37-1484), *t*-ZrO_2 (PDF #50-1089), and Ru (PDF #06-0663) are presented in the upper panel.

SiO_2. The volcano-shaped trends in the BET surface area and pore volume are very compatible with those found in the hydrogenation activity results and Ru particle size. Particularly, the uphill slope in these trends is quite understandable because amorphous SiO_2 in the vicinity of ZrO_2 can suppress the nucleation and growth of ZrO_2 particles and stabilize the tetragonal zirconia [39,57,58]. This would explain the decrease in Ru particle size of Ru/SZ-*x* catalysts and, accordingly, the improvement in their hydrogenation activity.

Thus, we focused on understanding the downhill slope in the BET surface area, pore volume, and hydrogenation activity (relevant to Ru particle size) observed in the catalysts containing more Si than Ru/SZ-5.0. According to our previous report that the particle size of Ru in Ru/ZrO_2 catalysts highly depends on the surface OH density of zirconium hydroxide [26], the surface compositions of Ru/SZ-*x* catalysts were acquired by XPS analysis. The Ru $3p_{3/2}$ peak is gradually lowered with the Si content increasing (Fig. 5(a)); the surface atomic ratio of Ru/(Si+Zr) decreases from 8.05 at% for Ru/SZ-0.0 to 4.48 at% for Ru/SZ-30.0 (Table 2). The surface enrichment of Ru can be explained from TPR-MS results for the as-impregnated $Ru_3(CO)_{12}$/SZ-*x*-d samples, where the carbonyl ligand coordinated to Ru species undergoes the methanation reaction with the H_2 fed during thermolysis [32]. For the sample with a higher Si/(Si+Zr), a peak corresponding to H_2 consumption was detected at lower temperatures (Fig. 5(b)). This suggests weaker interaction of $Ru_3(CO)_{12}$ with the surface of SZ-*x*-d sample with a higher *x* value.

Since the surface OH group of metal oxide supports significantly affects metal-support interaction derived by $Ru_3(CO)_{12}$ [13,30,31,59,60], the surface oxygen species of SZ-*x*-d samples was investigated by deconvolution of XPS O 1s spectra (Fig. S10). The binding energies corresponding to the surface OH groups, O^{2-} ions in the Zr-O-Zr lattice, and O^{2-} ions in the Zr-O-Si and Si-O-Si lattice are centered at 531.3, 529.7, and 532.4 eV, respectively [61-63]. As presented in Fig. 6(a), the fraction of surface OH group decreases from 73.8% (SZ-0.0-d) to 63.5% (SZ-30.0-d) and vice versa with that of bridging oxygen species [64]. When the XPS O 1s spectra of $Ru_3(CO)_{12}$/SZ-*x*-d samples were also examined (Fig. S11), the same trend as SZ-*x*-d samples was obtained, while the

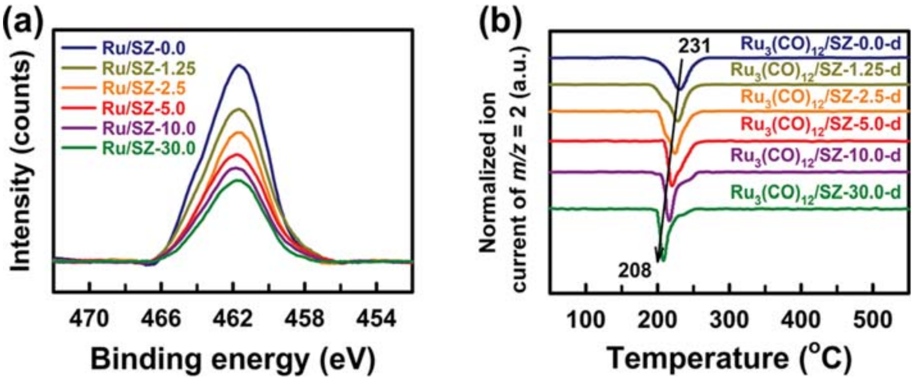

Fig. 5. (a) XPS Ru $3p_{3/2}$ spectra of Ru/SZ-*x* catalysts. (b) TPR-MS profiles of $Ru_3(CO)_{12}$/SZ-*x*-d samples for the mass fragment of *m/z*=2 indicating H_2 consumption.

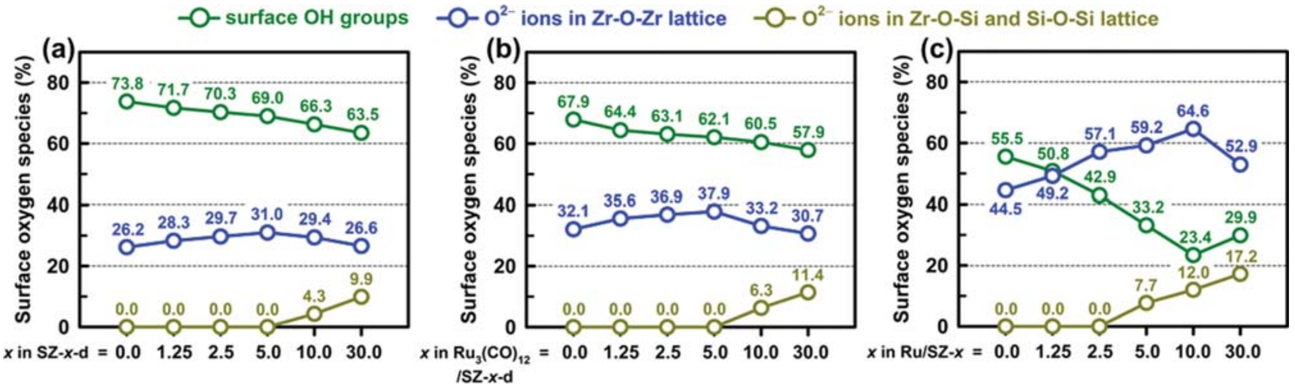

Fig. 6. Quantification of surface oxygen species calculated by the deconvolution of XPS O 1s spectra: (a) SZ-*x*-d samples, (b) $Ru_3(CO)_{12}$/SZ-*x*-d samples, and (c) Ru/SZ-*x* catalysts.

fraction of surface OH group was lower than that in SZ-*x*-d samples (Fig. 6(b)). The latter result is caused by oxidative addition of $Ru_3(CO)_{12}$ into the surface OH group of support during impregnation [29]. Moreover, the deconvolution of XPS O 1s spectra for Ru/SZ-*x* catalysts (Fig. S12) shows that the decrease in the fraction of surface OH group is remarkable with the Si content increasing (Fig. 6(c)) and the surface atomic value of O/(Si+Zr) is the same for all the Ru/SZ-*x* catalysts (Table 1). Notably, the surface OH group of Ru/SZ-30.0 is larger than that of Ru/SZ-10.0 due to the rod-like ZrO_2 structure formed by the aggregation of ZrO_2 at the surface. These results suggest that the increased heterogeneity by Si incorporation into ZrO_2 can destroy the surface charge balance due to the higher electronegativity of Si than Zr, thus resulting in the decrease in the surface area and pore volume of Ru/SZ-*x* catalysts with a higher *x* value than 5.0.

Therefore, the increase in the Si/(Si+Zr) ratio up to 5 mol% enhances thermal stability of tetragonal ZrO_2 in Ru/SZ-*x* catalysts, leading to the improvement of textural properties. However, the addition of more Si than 5 mol% Si/(Si+Zr) incurs the lower density of surface OH group by the collapsed charge balance, which imposes a negative effect on the textural properties and Ru particle. Due to these features, the hydrogenation activity and Ru particle size of Ru/SZ-*x* catalysts exhibit a volcano-shaped dependence on the Si content, where Ru/SZ-5.0 is believed to be the best catalyst. The aforementioned discussion is graphically presented in Fig. 7.

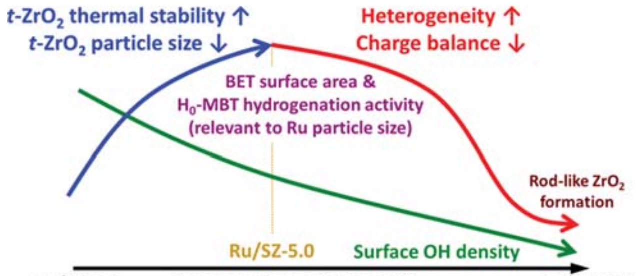

Fig. 7. Graphical illustration to represent the effects of Si/(Si+Zr) ratio on the properties and hydrogenation activity of Ru/SZ-*x* catalysts.

4. Characteristics of SZ-*x*-d and SZ-*x*-H_2-700 Samples

The physical properties of the as-prepared SZ-*x*-d and SZ-*x*-H_2-700 samples were investigated to confirm the characteristics observed in Ru/SZ-*x* catalysts, as listed in Table 3. From N_2 physisorption results of SZ-*x*-d samples (Fig. S13), the BET surface area is almost similar up to SZ-5.0-d (472-483 m^2 g^{-1}) but decreases to 419 m^2 g^{-1} by further addition of Si, while the pore volume and diameter is decreased with the increase in the Si content. Since all the SZ-*x*-d samples are of amorphous nature (not shown for brevity), their

Table 3. Physical properties of SZ-*x*-d and SZ-*x*-H_2-700 samples

Sample	S_{BET} [m^2 g^{-1}][a]	V_p [cm^3 g^{-1}][a]	d_p [nm][a]	$D_{m\text{-}ZrO_2}$ [nm][b]	$D_{t\text{-}ZrO_2}$ [nm][b]
SZ-0.0-d	472	0.48	4.1	-	-
SZ-1.25-d	478	0.44	3.7	-	-
SZ-2.5-d	480	0.41	3.4	-	-
SZ-5.0-d	483	0.40	3.3	-	-
SZ-10.0-d	453	0.31	2.7	-	-
SZ-30.0-d	419	0.27	2.5	-	-
SZ-0.0-H_2-700	16	0.05	11.8	28.2	34.5
SZ-1.25-H_2-700	35	0.08	8.9	17.6	19.7
SZ-2.5-H_2-700	50	0.09	6.9	-	16.2
SZ-5.0-H_2-700	97	0.09	3.7	-	13.8
SZ-10.0-H_2-700	74	0.06	3.4	-	12.6
SZ-30.0-H_2-700	50	0.02	1.7	-	10.6

[a] BET surface area (S_{BET}), pore volume (V_p), and pore diameter (d_p) measured by N_2 physisorption at 77 K.
[b] Particle size of monoclinic ZrO_2 ($D_{m\text{-}ZrO_2}$) and tetragonal ZrO_2 ($D_{t\text{-}ZrO_2}$) calculated by the Scherrer's equation.

textural properties would be hardly affected by the incorporation of Si into ZrO_2 up to the Si/(Si+Zr) of 5 mol%.

Thus, SZ-*x*-H_2-700 samples were characterized by N_2 physisorption (BET isotherms and pore size distribution curves in Fig. S14), because they are subjected to the heat treatment identical to Ru/SZ-*x* catalysts. The measured BET surface area and pore volume are in a volcano-shaped relationship with the Si content at the maximum with SZ-5.0-H_2-700 (97 m^2 g^{-1} and 0.091 cm^3 g^{-1}). Also, the XRD patterns of SZ-*x*-H_2-700 samples show a similar change in ZrO_2 phase identified for Ru/SZ-*x* catalysts: *m*-ZrO_2 and *t*-ZrO_2 are observed in SZ-0.0-H_2-700 and SZ-1.25-H_2-700, but only the latter phase is detected from SZ-2.5-H_2-700 (Fig. S15). In addition, the particle size of *t*-ZrO_2 continuously decreases from 34.5 nm for SZ-0.0-H_2-700 to 10.6 nm for SZ-30.0-H_2-700 (Table 3), which is also confirmed in Ru/SZ-*x* catalysts. The good agreement between SZ-*x*-H_2-700 samples and Ru/SZ-*x* catalysts indicates that the charge imbalance in the SZ-*x*-d samples becomes dominant by heat treatment. Particularly, when $Ru_3(CO)_{12}$ is loaded onto the SZ-*x*-d samples, this outcome will be strengthened by aid of their surface OH density.

CONCLUSIONS

We investigated the effect of Si addition into ZrO_2 on the physicochemical properties and hydrogenation activity of Ru/SZ-*x* catalysts prepared by thermolysis of $Ru_3(CO)_{12}$ loaded onto SZ-*x*-d samples. The Zr-O-Si bond formed by the incorporation of Si into ZrO_2 enhanced the thermal stability and decreased the particle size of *t*-ZrO_2. However, the density of the surface OH group was reduced with the Si content increasing, due to charge imbalance induced by the increased heterogeneity. From the combination of these features, the textural properties of Ru/SZ-*x* catalysts are in a volcano-shaped relationship with the Si content, where the best is achieved at the Si/(Si+Zr) ratio of 5 mol%. Moreover, the same tendency is observed in the Ru particle size and H_2 storage efficiency of Ru/SZ-*x* catalysts with the highest activity and smallest Ru particles in Ru/SZ-5.0. Overall, the thermal stability and surface OH density of SZ-*x*-d samples play a pivotal role in the physicochemical properties and hydrogenation activity of Ru/SZ-*x* catalysts. Consequently, the hydrogenation activity of Ru/ZrO_2 catalyst can be enhanced by the addition of up to 5 mol% Si into ZrO_2.

ACKNOWLEDGEMENTS

This work was financially supported by the National Research Foundation of Korea (NRF) funded by the Ministry of Science and ICT, Republic of Korea (NRF-2019M3E6A1064908), and by the Ministry of Education, Republic of Korea (NRF-2016R1A6A1A03013422).

SUPPORTING INFORMATION

Additional information as noted in the text. This information is available via the Internet at http://www.springer.com/chemistry/journal/11814.

REFERENCES

1. D. Geburtig, P. Preuster, A. Bösmann, K. Müller and P. Wasserscheid, *Int. J. Hydrogen Energy*, **41**, 1010 (2016).
2. P. Preuster, C. Papp and P. Wasserscheid, *Acc. Chem. Res.*, **50**, 74 (2017).
3. P. T. Aakko-Saksa, C. Cook, J. Kiviaho and T. Repo, *J. Power Sources*, **396**, 803 (2018).
4. G. Sievi, D. Geburtig, T. Skeledzic, A. Bösmann, P. Preuster, O. Brummel, F. Waidhas, M. A. Montero, P. Khanipour, I. Katsounaros, J. Libuda, K. J. J. Mayrhofer and P. Wasserscheid, *Energy Environ. Sci.*, **12**, 2305 (2019).
5. K. Müller, S. Thiele and P. Wasserscheid, *Energy Fuels*, **33**, 10324 (2019).
6. M. Markiewicz, Y. Q. Zhang, A. Bösmann, N. Brückner, J. Thöming, P. Wasserscheid and S. Stolte, *Energy Environ. Sci.*, **8**, 1035 (2015).
7. H. Jorschick, P. Preuster, S. Dürr, A. Seidel, K. Müller, A. Bösmann and P. Wasserscheid, *Energy Environ. Sci.*, **10**, 1652 (2017).

8. M. Niermann, S. Drünert, M. Kaltschmitt and K. Bonhoff, *Energy Environ. Sci.*, **12**, 290 (2019).
9. M. Niermann, A. Beckendorff, M. Kaltschmitt and K. Bonhoff, *Int. J. Hydrogen Energy*, **44**, 6631 (2019).
10. P. M. Modisha, C. N. M. Ouma, R. Garidzirai, P. Wasserscheid and D. Bessarabov, *Energy Fuels*, **33**, 2778 (2019).
11. N. Brückner, K. Obesser, A. Bösmann, D. Teichmann, W. Arlt, J. Dungs and P. Wasserscheid, *ChemSusChem*, **7**, 229 (2014).
12. A. Leinweber and K. Müller, *Energy Technol.*, **6**, 513 (2018).
13. T. W. Kim, S. H. Ko, M. Kim and Y.-W. Suh, *Adv. Powder Technol.*, **31**, 1682 (2020).
14. J. Oh, T. W. Kim, K. Jeong, J. H. Park and Y.-W. Suh, *ChemCatChem*, **10**, 3892 (2018).
15. J. Oh, H. B. Bathula, J. H. Park and Y.-W. Suh, *Commun. Chem.*, **2**, 68 (2019).
16. F. Auer, D. Blaumeiser, T. Bauer, A. Bösmann, N. Szesni, J. Libuda and P. Wasserscheid, *Catal. Sci. Technol.*, **9**, 3537 (2019).
17. P. T. Aakko-Saksa, M. Vehkamäki, M. Kemell, L. Keskiväli, P. Simell, M. Reinikainen, U. Tapper and T. Repo, *Chem. Commun.*, **56**, 1657 (2020).
18. S. Dürr, M. Müller, H. Jorschick, M. Helmin, A. Bösmann, R. Palkovits and P. Wasserscheid, *ChemSusChem*, **10**, 42 (2017).
19. H. Jorschick, A. Bösmann, P. Preuster and P. Wasserscheid, *ChemCatChem*, **10**, 4329 (2018).
20. H. Jorschick, A. Bulgarin, L. Alletsee, P. Preuster, A. Bösmann and P. Wasserscheid, *ACS Sustainable Chem. Eng.*, **7**, 4186 (2019).
21. H. Jorschick, M. Vogl, P. Preuster, A. Bösmann and P. Wasserscheid, *Int. J. Hydrogen Energy*, **44**, 31172 (2019).
22. L. Li, M. Yang, Y. Dong, P. Mei and H. Cheng, *Int. J. Hydrogen Energy*, **41**, 16129 (2016).
23. J. Oh, K. Jeong, T. W. Kim, H. Kwon, J. W. Han, J. H. Park and Y.-W. Suh, *ChemSusChem*, **11**, 661 (2018).
24. M. Jang, Y. S. Jo, W. J. Lee, B. S. Shin, H. Sohn, H. Jeong, S. C. Jang, S. K. Kwak, J. W. Kang and C. W. Yoon, *ACS Sustainable Chem. Eng.*, **7**, 1185 (2019).
25. J. Álvarez-Rodríguez, A. Guerrero-Ruiz, I. Rodríguez-Ramos and A. Arcoya-Martín, *Catal. Today*, **107-108**, 302 (2005).
26. T. W. Kim, S. Park, J. Oh, C.-H. Shin and Y.-W. Suh, *ChemCatChem*, **10**, 3406 (2018).
27. V. L. Kuznetsov, A. T. Bell and Y. I. Yermakov, *J. Catal.*, **65**, 374 (1980).
28. A. Zecchina, E. Guglielminotti, A. Bossi and M. Camia, *J. Catal.*, **74**, 225 (1982).
29. J. M. Basset and A. Choplin, *J. Mol. Catal.*, **21**, 95 (1983).
30. K. Asakura, K.-K. Bando and Y. Iwasawa, *J. Chem. Soc., Faraday Trans.*, **86**(14), 2645 (1990).
31. K. Asakura and Y. Iwasawa, *J. Chem. Soc., Faraday Trans.*, **86**(14), 2657 (1990).
32. T. W. Kim, J. Oh and Y.-W. Suh, *Appl. Catal. A: Gen.*, **547**, 183 (2017).
33. T. Bhaskar, K. R. Reddy, C. P. Kumar, M. R. V. S. Murthy and K. V. R. Chary, *Appl. Catal. A: Gen.*, **211**, 189 (2001).
34. G. Zhou, X. Tan, Y. Pei, K. Fan, M. Qiao, B. Sun and B. Zong, *ChemCatChem*, **5**, 2425 (2013).
35. D. Rao, X. Xue, G. Cui, S. He, M. Xu, W. Bing, S. Shi and M. Wei, *Catal. Sci. Technol.*, **8**, 236 (2018).
36. A. M. Ruppert, M. Niewiadomski, J. Grams and W. Kwapiński, *Appl. Catal. B: Environ.*, **145**, 85 (2014).
37. E. Hong, C. Kim, D.-H. Lim, H.-J. Cho and C.-H. Shin, *Appl. Catal. B: Environ.*, **232**, 544 (2018).
38. H. J. M. Bosman, E. C. Kruissink, J. van der Spoel and F. van den Brink, *J. Catal.*, **148**, 660 (1994).
39. F. del Monte, W. Larsen and J. D. Mackenzie, *J. Am. Ceram. Soc.*, **83**(6), 1506 (2000).
40. D. H. Aguilar, L. C. Torres-Gonzalez, L. M. Torres-Martinez, T. Lopez and P. Quintana, *J. Solid State Chem.*, **158**, 349 (2000).
41. S. Pyen, E. Hong, M. Shin, Y.-W. Suh and C.-H. Shin, *Mol. Catal.*, **448**, 71 (2018).
42. L. Han, D. Mao, J. Yu, Q. Guo and G. Lu, *Appl. Catal. A: Gen.*, **454**, 81 (2013).
43. J. Gu, Z. Xin, M. Tao, Y. Lv, W. Gao and Q. Si, *Appl. Catal. A: Gen.*, **575**, 230 (2019).
44. G. K. Reddy, S. Loridant, A. Takahashi, P. Delichère and B. M. Reddy, *Appl. Catal. A: Gen.*, **389**, 92 (2010).
45. B. Stolze, J. Titus, S. A. Schunk, A. Milanov, E. Schwab and R. Gläser, *Front. Chem. Sci. Eng.*, **10**(2), 281 (2016).
46. X. Zhang, Q. Zhang, T. Wang, L. Ma, Y. Yu and L. Chen, *Bioresour. Technol.*, **134**, 73 (2013).
47. S. Foraita, Y. Liu, G. L. Haller, E. Baráth, C. Zhao and J. A. Lercher, *ChemCatChem*, **9**, 195 (2017).
48. G. Perera and R. H. Doremus, *J. Am. Ceram. Soc.*, **74**(7), 1554 (1991).
49. S. Sato, R. Takahashi, T. Sodesawa, S. Tanaka, K. Oguma and K. Ogura, *J. Catal.*, **196**, 190 (2000).
50. S. Damyanova, P. Grange and B. Delmon, *J. Catal.*, **168**, 421 (1997).
51. W. Wang, J. Zhou, D. Wei, H. Wan, S. Zheng, Z. Xu and D. Zhu, *J. Colloid Interface Sci.*, **407**, 442 (2013).
52. T. Lopez, J. Navarrete, R. Gomez, O. Novaro, F. Figueras and H. Armendariz, *Appl. Catal. A: Gen.*, **125**, 217 (1995).
53. S. Kongwudthiti, P. Praserthdam, W. Tanakulrungsank and M. Inoue, *J. Mater. Process. Technol.*, **136**, 186 (2003).
54. Y. Kuwahara, W. Kaburagi, K. Nemoto and T. Fujitani, *Appl. Catal. A: Gen.*, **476**, 186 (2014).
55. G. Monrós, M. C. Martí, J. Carda, M. A. Tena, P. Escribano and M. Anglada, *J. Mater. Sci.*, **28**, 5852 (1993).
56. J. B. Miller and E. I. Ko, *J. Catal.*, **159**, 58 (1996).
57. F. del Monte, W. Larsen and J. D. Mackenzie, *J. Am. Ceram. Soc.*, **83**(3), 628 (2000).
58. V. S. Nagarajan and K. J. Rao, *J. Mater. Sci.*, **24**, 2140 (1989).
59. J. G. Goodwin Jr. and C. Naccache, *Appl. Catal.*, **4**, 145 (1982).
60. H. H. Lamb, B. C. Gates and H. Knözinger, *Angew. Chem. Int. Ed. Engl.*, **27**, 1127 (1988).
61. J.-W. Lee, S. Kong, W.-S. Kim and J. Kim, *Mater. Chem. Phys.*, **106**, 39 (2007).
62. C. Ren, W. Qiu and Y. Chen, *Sep. Purif. Technol.*, **107**, 264 (2013).
63. J.-H. Lee, C.-H. Shin and Y.-W. Suh, *Mol. Catal.*, **438**, 272 (2017).
64. C. Flego, L. Carluccio, C. Rizzo and C. Perego, *Catal. Commun.*, **2**, 43 (2001).

Supporting Information

Hydrogen storage into monobenzyltoluene over Ru catalyst supported on SiO_2-ZrO_2 mixed oxides with different Si/Zr ratios

Tae Wan Kim*, Chansong Kim, Hwiram Jeong*, Chae-Ho Shin**, and Young-Woong Suh*,***,†**

*Department of Chemical Engineering, Hanyang University, Seoul 04763, Korea
**Department of Chemical Engineering, Chungbuk National University, Chungbuk 28644, Korea
***Research Institute of Industrial Science, Hanyang University, Seoul 04763, Korea
(*Received 1 April 2020 • Revised 29 April 2020 • Accepted 11 May 2020*)

Table S1. Hydrogenation activity results of Ru/SZ-*x* catalysts[a]

Sample	Temp. [°C]	Catalyst amount [mg]	Conversion of H_0-MBT [%]	Selectivity [%]				H_2 storage efficiency [%]
				H_{12}-MBT	H_{10}-MBT	H_6-MBT	H_4-MBT	
Ru/SZ-0.0	150	120	62.2	7.1	5.1	75.4	12.4	33.1
	170	120	71.5	7.8	4.6	79.0	8.5	38.6
	170	200	90.9	13.6	4.4	79.3	2.6	52.7
Ru/SZ-1.25	150	120	69.8	8.0	4.9	78.7	8.5	37.9
	170	120	76.8	9.6	3.5	80.6	6.3	42.1
	170	200	96.7	17.8	5.1	76.0	1.1	58.4
Ru/SZ-2.5	150	120	88.0	9.3	5.4	78.3	7.1	45.3
	170	120	88.4	10.7	4.9	80.8	3.6	49.8
	170	200	100.0	47.5	7.9	44.6	0.0	76.4
Ru/SZ-5.0	150	120	92.8	16.3	4.8	76.4	2.5	55.1
	170	120	100.0	27.5	5.3	67.2	0.0	65.5
	170	200	100.0	91.3	4.7	4.0	0.0	97.2
Ru/SZ-10.0	150	120	86.8	13.0	4.1	79.6	3.2	49.7
	170	120	95.5	17.3	3.9	77.8	1.0	57.1
	170	200	100.0	59.5	8.3	32.2	0.0	82.5
Ru/SZ-30.0	150	120	43.8	7.1	4.3	80.8	7.8	23.6
	170	120	55.7	7.9	3.1	84.9	4.1	30.3
	170	200	87.9	15.1	3.3	80.4	1.1	51.3

[a] Reaction conditions: reaction system A, 15 g H_0-MBT, 50 bar H_2, 1,200 rpm, and 2 h.

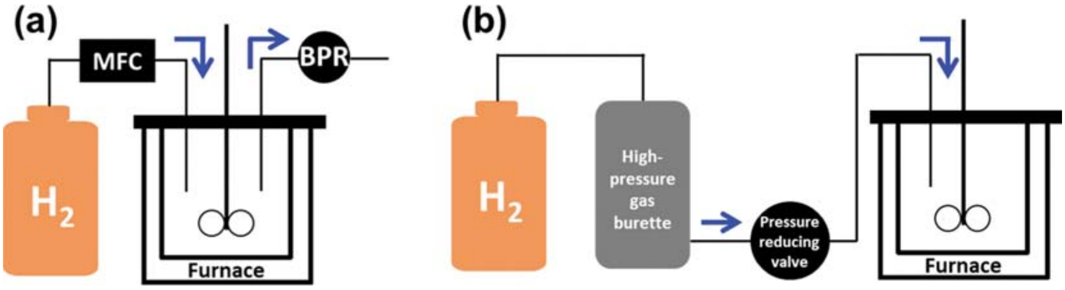

Fig. S1. Schematic illustration of two different manners for the hydrogenation of H_0-MBT in a Parr reactor: (a) Reaction system A and (b) reaction system B.

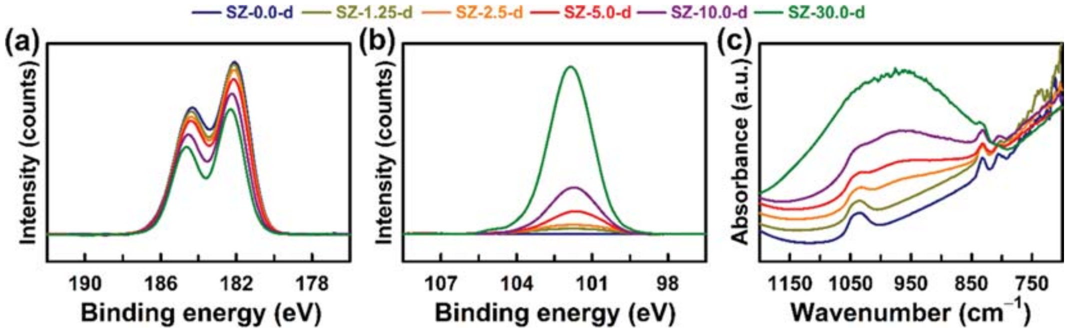

Fig. S2. XPS and FT-IR spectra of SZ-*x*-d samples: (a) XPS Zr 3d, (b) XPS Si 2p, and (c) FT-IR.

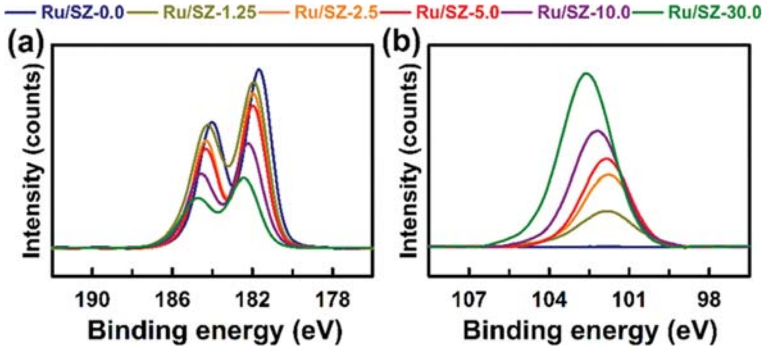

Fig. S3. XPS spectra of Ru/SZ-*x* catalysts: (a) XPS Zr 3d and (b) XPS Si 2p.

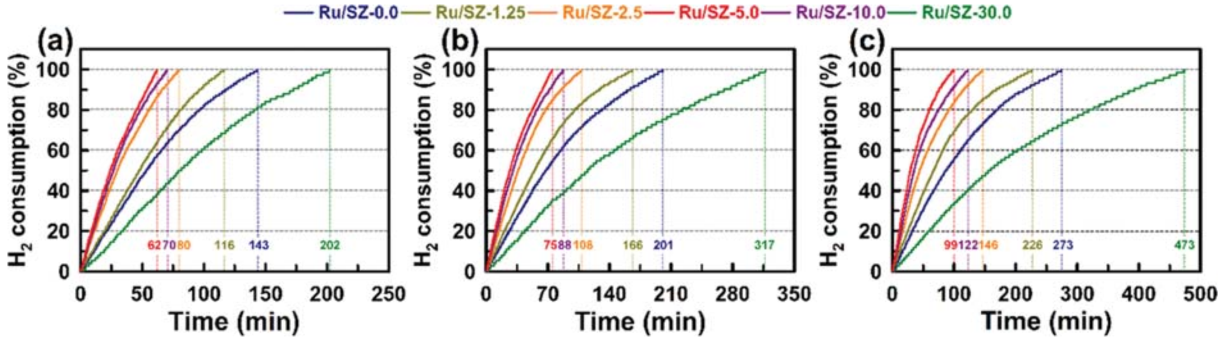

Fig. S4. H_2 consumption curves in the hydrogenation of H_0-MBT over Ru/SZ-*x* catalysts using the reaction system B. Reaction conditions: 10 g H_0-MBT, 50 bar H_2, 200 mg$_{cat}$, 1,200 rpm, and temperature of (a) 210 °C, (b) 190 °C, and (c) 170 °C.

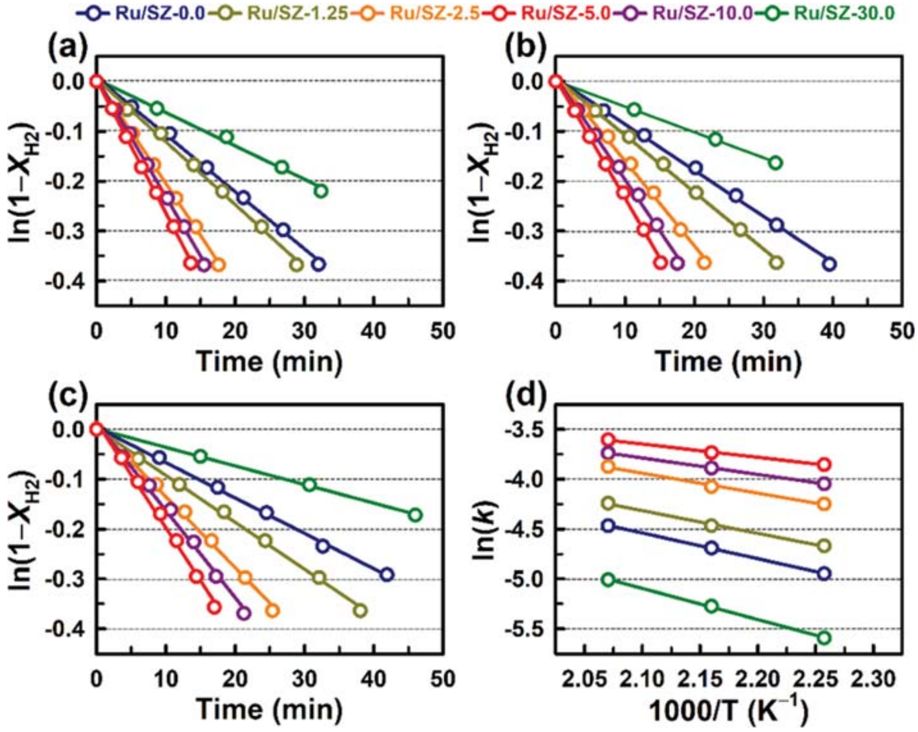

Fig. S5. (a)-(c) Plots for calculating the rate constants from the activty results presented in Fig. S3 at the temperature of (a) 210 °C, (b) 190 °C, and (c) 170 °C. (d) Plot for calculating the activation energy in the Arrhenius plot.

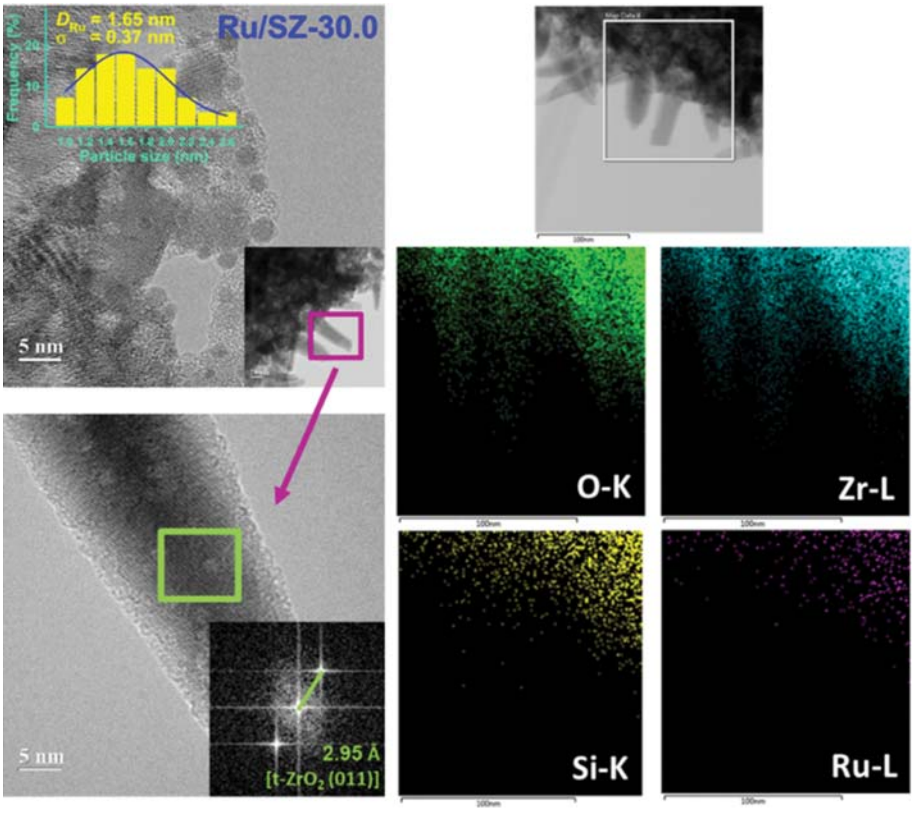

Fig. S6. HR-TEM images and TEM-EDS mapping images of Ru/SZ-30.0.

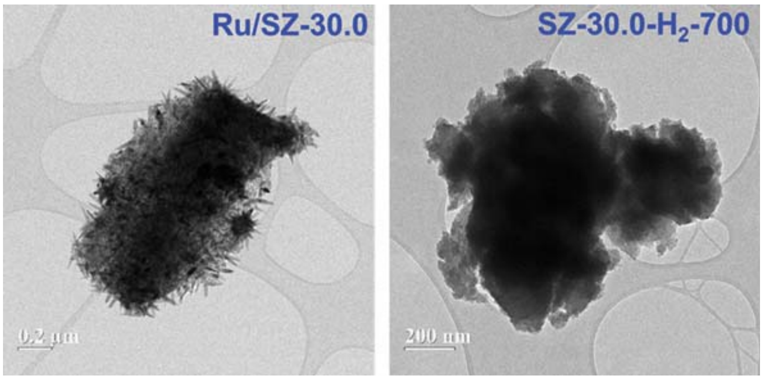

Fig. S7. TEM images of Ru/SZ-30.0 and SZ-30.0-H$_2$-700.

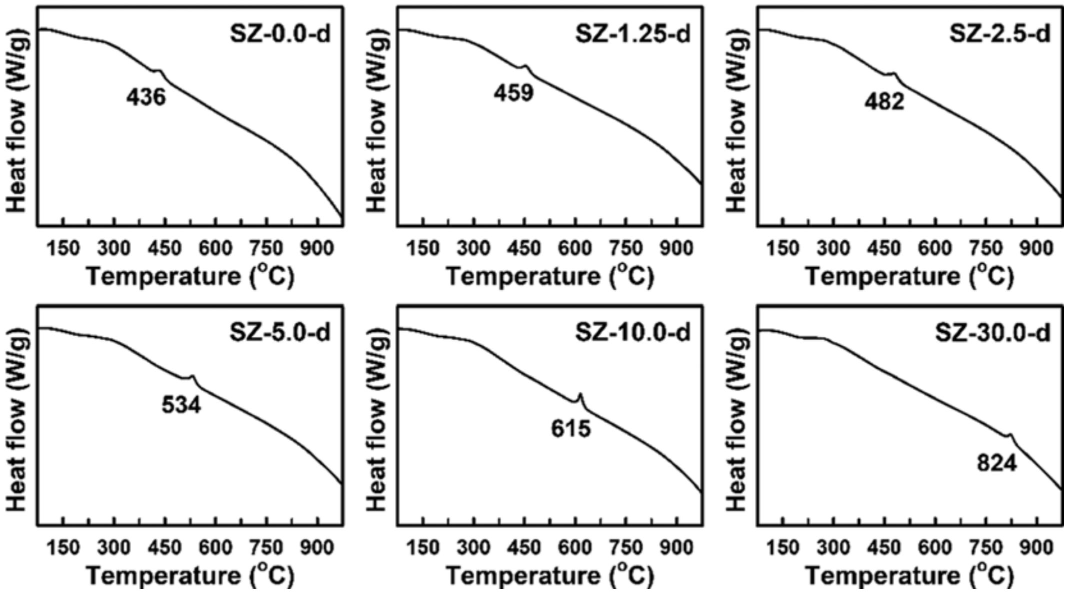

Fig. S8. DSC curves of SZ-*x*-d samples.

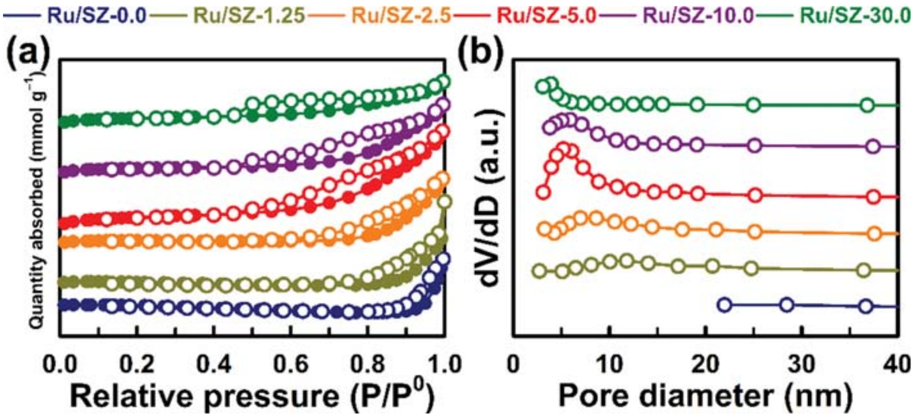

Fig. S9. N$_2$ physisorption results of Ru/SZ-*x* catalysts: (a) N$_2$ adsorption-desorption isotherms and (b) pore size distribution curves.

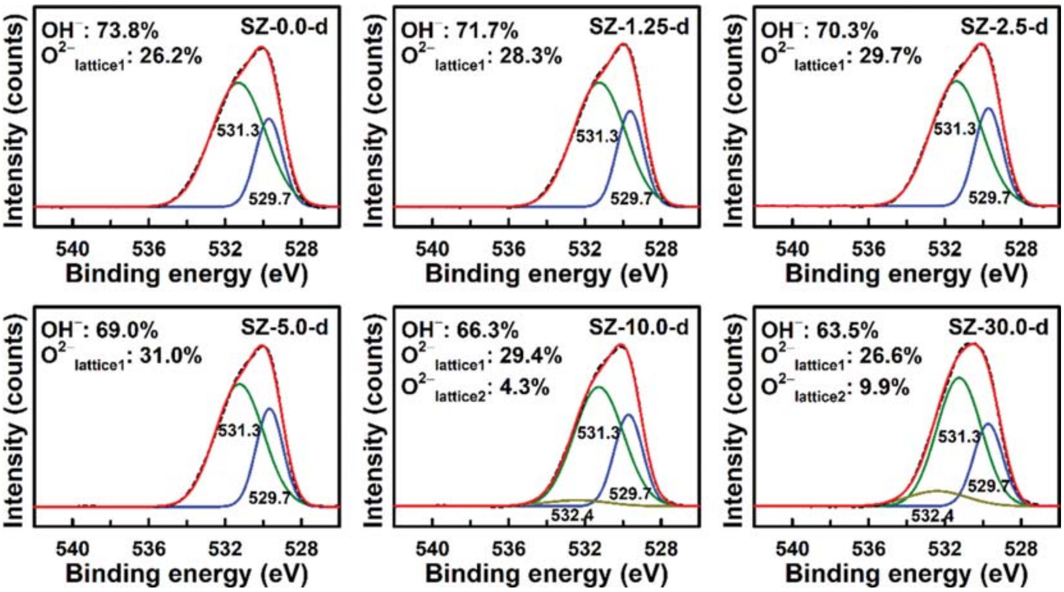

Fig. S10. XPS O 1s spectra of SZ-*x*-d samples. The red curves represent the total fitting curve for individual splitted peaks, while the green, blue, and yellow curves represent surface OH groups of the support, O^{2-} ions in the Zr-O-Zr lattice, and O^{2-} ions in the Zr-O-Si and Si-O-Si lattice, respectively.

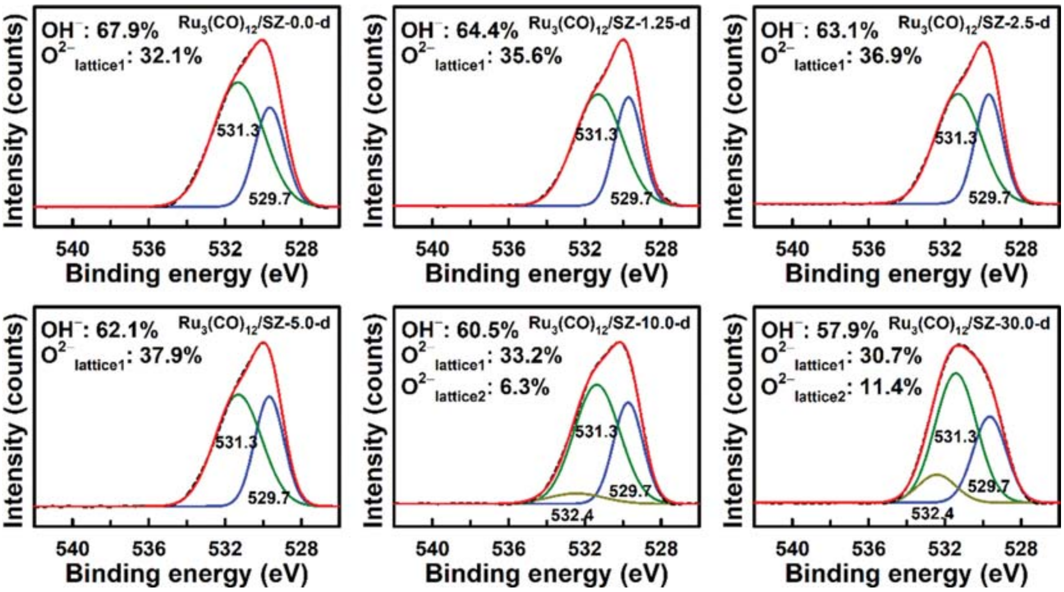

Fig. S11. XPS O 1s spectra of $Ru_3(CO)_{12}$/SZ-*x*-d samples. The red curves represent the total fitting curve for individual splitted peaks, while the green, blue, and yellow curves represent surface OH groups of the support, O^{2-} ions in the Zr-O-Zr lattice, and O^{2-} ions in the Zr-O-Si and Si-O-Si lattice, respectively.

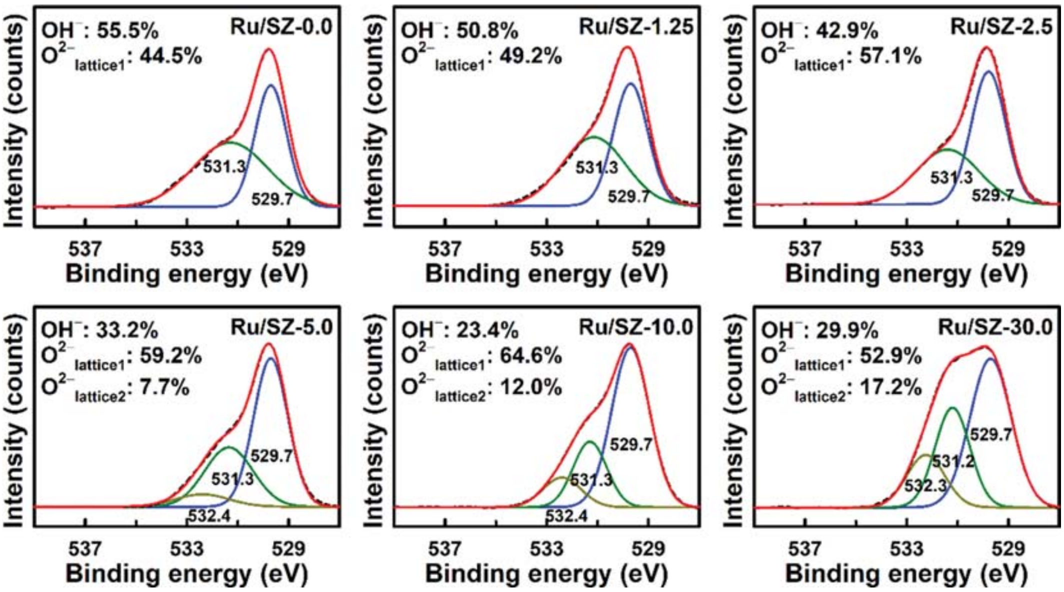

Fig. S12. XPS O 1s spectra of Ru/SZ-*x* catalysts. The red curves represent the total fitting curve for individual splitted peaks, while the green, blue, and yellow curves represent surface OH groups of the support, O^{2-} ions in the Zr-O-Zr lattice, and O^{2-} ions in the Zr-O-Si and Si-O-Si lattice, respectively.

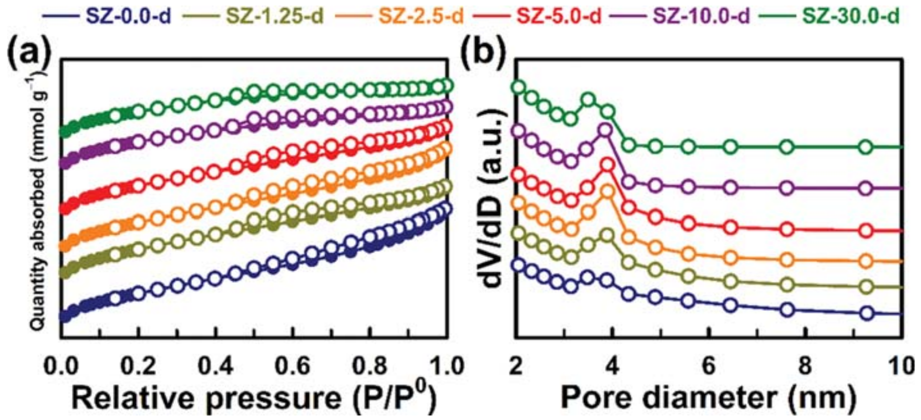

Fig. S13. N_2 physisorption results of SZ-*x*-d samples: (a) N_2 adsorption-desorption isotherms and (b) pore size distribution curves.

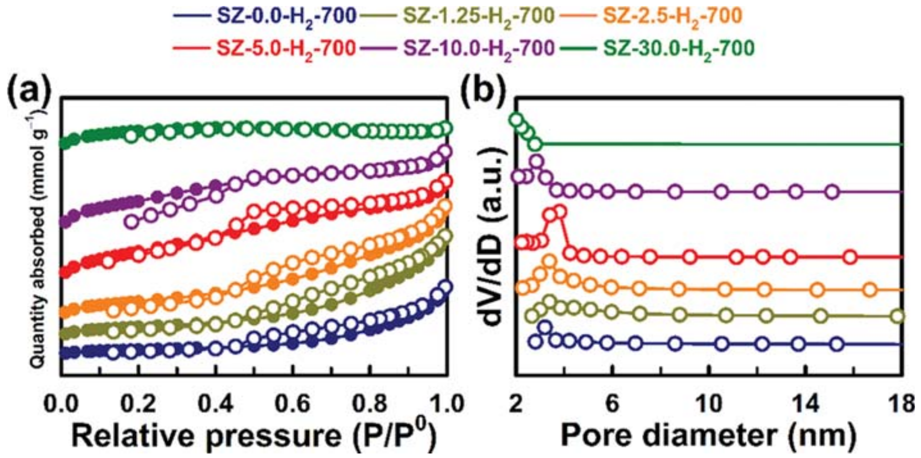

Fig. S14. N_2 physisorption results of SZ-*x*-H_2-700 samples: (a) N_2 adsorption-desorption isotherms and (b) pore size distribution curves.

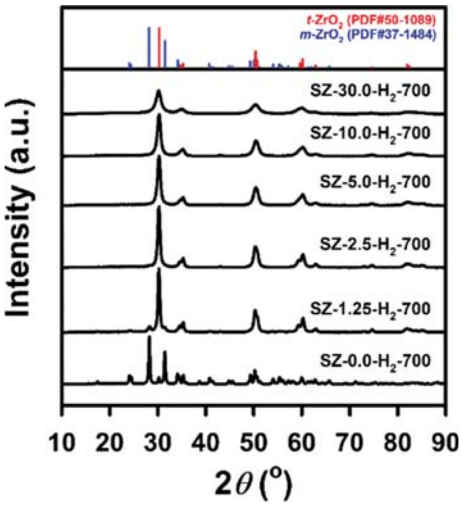

Fig. S15. XRD patterns of SZ-*x*-H_2-700 samples with the reflections of monoclinic ZrO_2 (*m*-ZrO_2) (PDF #37-1484) and tetragonal ZrO_2 (*t*-ZrO_2) (PDF #50-1089).